Supporting Information for
Underestimated MJO in CMIP6 models

Phong V.V. Le[1,2], Clément Guilloteau[1], Antonios Mamalakis[1,3], and Efi Foufoula-Georgiou[1,4]

[1]Department of Civil and Environmental Engineering, University of California Irvine, CA, USA

[2]Faculty of Hydrology Meteorology and Oceanography, University of Science, Vietnam National University, Hanoi, Vietnam

[3]Department of Atmospheric Science, Colorado State University, Fort Collins, CO, USA

[4]Department of Earth Systems Science, University of California Irvine, CA, USA

Contents of this file

Table S1: The selected 20 CMIP6 models used in our study with names**,** institutions and horizontal grid resolution of the atmospheric and ocean variables. The models were selected based on data availability at the time of writing the manuscript. The ID assigned to each model is used throughout this study.

ID	Model	Institution Name	Average grid resolution (longitude x latitude)	
			Atmosphere	**Ocean**
1	ACCESS-CM2	Commonwealth Scientific and Industrial Research Organisation (CSIRO), Australia	1.87° × 1.25°	1.0° × 1.0°
2	ACCESS-ESM1-5		1.87° × 1.25°	1.0° × 1.0°
3	BCC-CSM2-MR	Beijing Climate Center, Beijing, China	1.1° × 1.1°	1.0° × 0.78°
4	BCC-ESM1		2.8° × 2.8°	1.0° × 0.78°
5	CanESM5	Canadian Centre for Climate Modelling and Analysis, Environment and Climate Change Canada, BC, Canada	2.8° × 2.8°	1.0° × 0.62°
6	CESM2	National Center for Atmospheric Research, Boulder, CO, USA	0.9° × 1.25°	0.9° × 1.25°
7	CESM2-FV2		1.9 ° × 2.5°	1.9° × 2.5°
8	CESM2-WACCM		0.9° × 1.25°	0.9° × 1.25°
9	CESM2-WACCM-FV2		1.9° × 2.5°	1.9° × 2.5°
10	EC-Earth3	Consortium of various institutions from Spain, Italy, Denmark, Finland, Germany, Ireland, Portugal, Netherlands, Norway, the United Kingdom, Belgium, and Sweden	0.7° × 0.7°	1.0° × 0.62°
11	EC-Earth3-Veg		0.7° × 0.7°	1.0° × 0.62°
12	GFDL-CM4	Geophysical Fluid Dynamics Laboratory, NOAA, Princeton, NJ, USA	1.0° × 1.0°	0.25° × 0.16°
13	IPSL-CM6A-LR	Institut Pierre Simon Laplace, Paris, France	2.5° × 1.25°	1.0° × 0.54°
14	MIROC6	Japan Agency for Marine-Earth Science and Technology, Atmosphere and Ocean Research Institute, National Institute for Environmental Studies, and RIKEN Center for Computational Science, Japan	1.4° × 1.4°	1.0° × 0.70°
15	MPI-ESM-1-2-HAM	Max Planck Institute fur Meteorologie, Forschungszentrum Julich, University of Oxford, Finnish Meteorological Institute, Leibniz Institute for Tropospheric Research, ETH Zurich	1.87° × 1.87°	1.52° × 0.82°
16	MPI-ESM1-2-HR		0.94° × 0.94°	0.45° × 0.45°
17	MPI-ESM1-2-LR		1.87° × 1.87°	1.4° × 0.82°
18	MRI-ESM2-0	Meteorological Research Institute, Tsukuba, Japan	1.1° × 1.1°	1.0° × 0.5°
19	NESM3	Nanjing University of Information Science and Technology, Nanjing, China	1.87° × 1.87°	1.0° × 0.62°
20	SAM0-UNICON	Seoul National University, Seoul, Republic of Korea	1.25° × 0.94°	1.1° × 0.47°

Table S2: List of observed daily global precipitation products used for comparison.

ID	Name	Abbreviation	Period of record	Spatial resolution
1	Precipitation Estimation from Remotely Sensed Information using Artificial Neural Networks - Climate Data Record	PERSIANN-CDR	1983-present	$0.25^{o} \times 0.25^{o}$
2	Integrated Multi-satellitE Retrievals for GPM	IMERG	2001-present	$0.1^{o} \times 0.1^{o}$
3	Tropical Rainfall Measuring Mission (34B2)	TRMM	1998-present	$0.25^{o} \times 0.25^{o}$
4	Global Precipitation Climatology Project	GPCP	1996- present	$1.0^{o} \times 1.0^{o}$
5	CPC MORPHing technique	CMORPH	2002- present	$0.25^{o} \times 0.25^{o}$

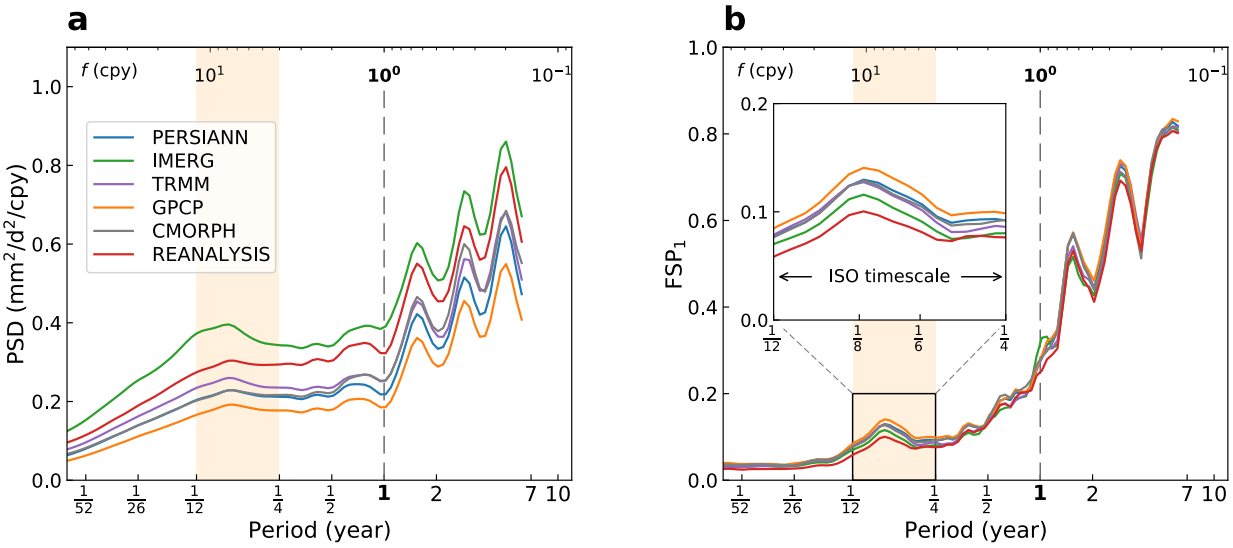

Figure S1. (a) Power spectral density and (b) Fraction of spectral power explained by the first wavelet principal component (wPC1) of daily precipitation rate obtained from 5 different observed datasets and the reanalysis products during the common period 2002-2019. The highest and lowest values of power spectral density is found in the IMERG and GPCP, respectively, but all observed datasets are in good agreement in terms of capturing the MJO mode. Frequency f in cycles per year (cpy) is shown in the top horizontal axes. The timescale corresponding to intra-seasonal oscillations (ISO; yellow shaded vertical bands) ranges from 1-3 months ($4 \leq f \leq 12$ cpy)

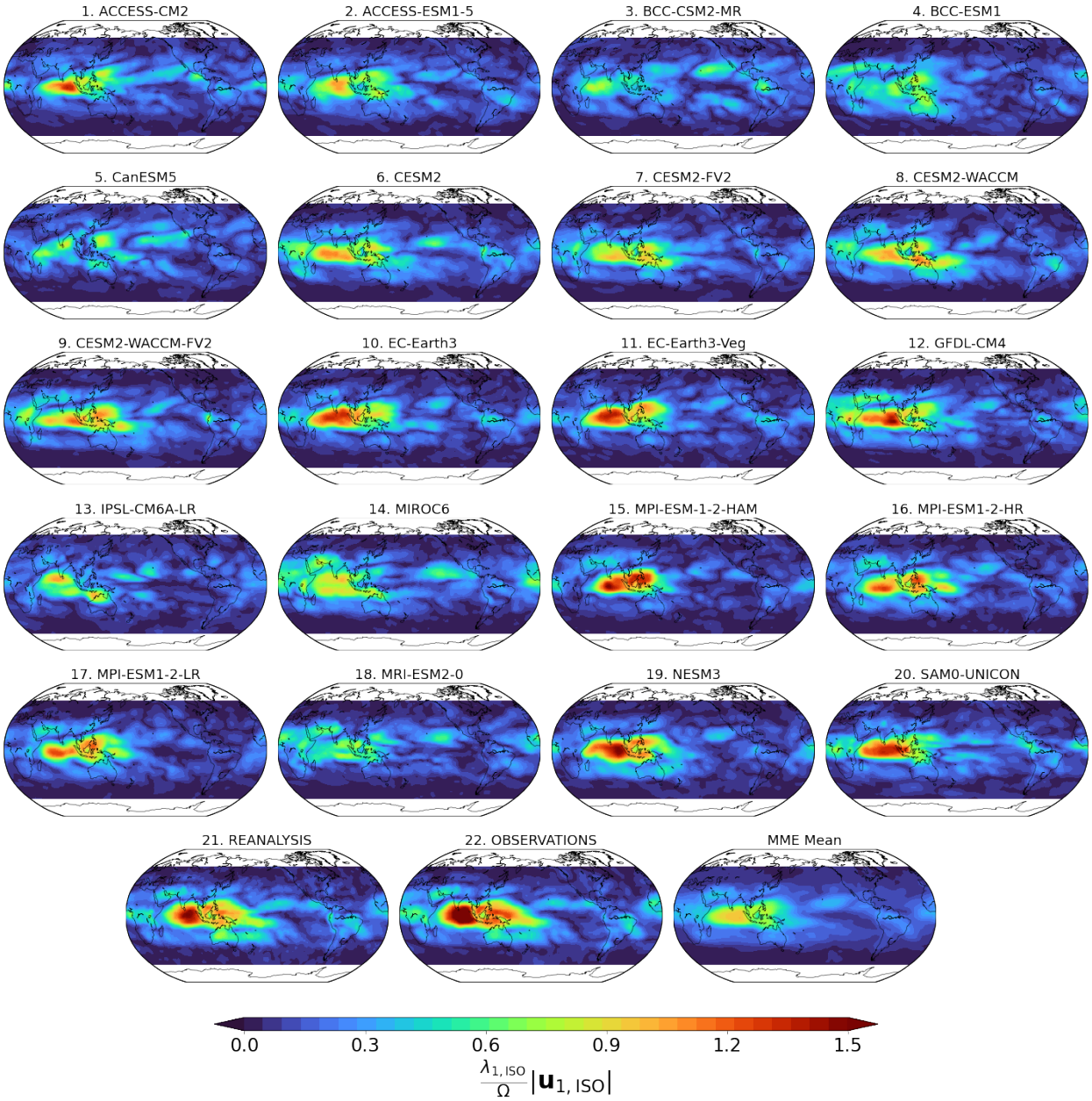

Figure S2. Spatial patterns of the modulus (magnitude) of the ISO band-integrated first complex eigenvector $\boldsymbol{u}_{1,\mathrm{ISO}}$ of OLR, corresponding to MJO, for the 20 CMIP6 models, reanalysis, and observations. The MME Mean represents the mean of the 20 models. The map is shown for the unit-norm eigenvector with a scaling factor $\frac{\lambda_{1,\mathrm{ISO}}}{\Omega}$ representing the contribution of wPC1 to the total energy in the ISO frequency band, with $\Omega = \sqrt{tr(\boldsymbol{\Lambda}_{\mathrm{ISO}})/N}$.

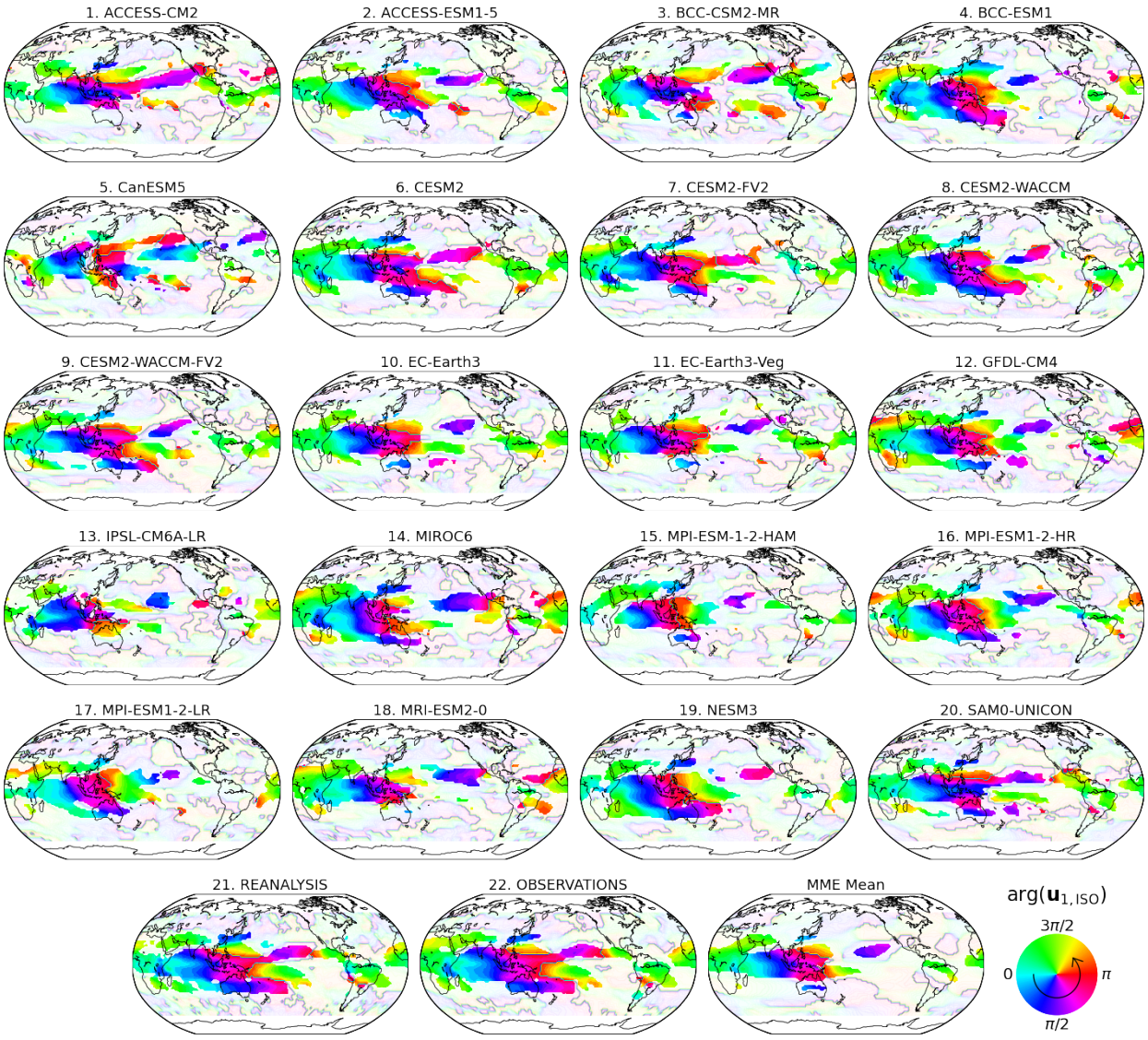

Figure S3. Spatial patterns of the argument (phase) of the ISO band-integrated first complex eigenvector $\boldsymbol{u}_{1,\mathrm{ISO}}$ of OLR, representing MJO propagation, for 20 CMIP6 models, reanalysis, and observations. The MME Mean represents the mean of 20 models. The counter-clockwise, circular arrow in the colorscale indicates the direction of propagation of the extracted waves.

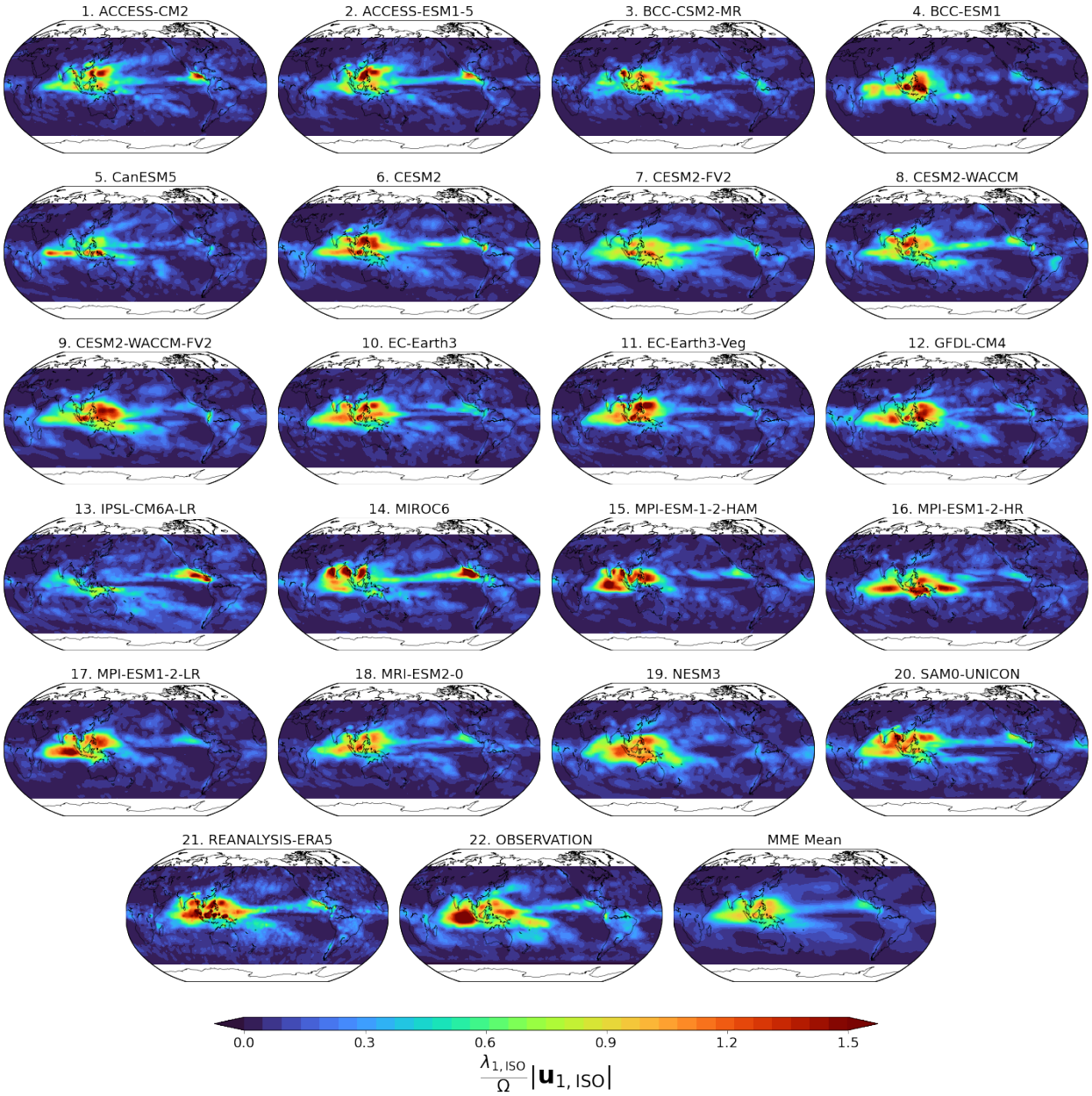

Figure S4. Spatial patterns of the modulus (magnitude) of the ISO band-integrated first complex eigenvector $\boldsymbol{u}_{1,\mathrm{ISO}}$ of PPT, corresponding to MJO, for the 20 CMIP6 models, reanalysis, and observations. The MME Mean represents the mean of the 20 models. The map is shown for the unit-norm eigenvector with a scaling factor $\frac{\lambda_{1,\mathrm{ISO}}}{\Omega}$ representing the contribution of wPC1 to the total energy in ISO frequency band, with $\Omega = \sqrt{tr(\boldsymbol{\Lambda}_{\mathrm{ISO}})/N}$.

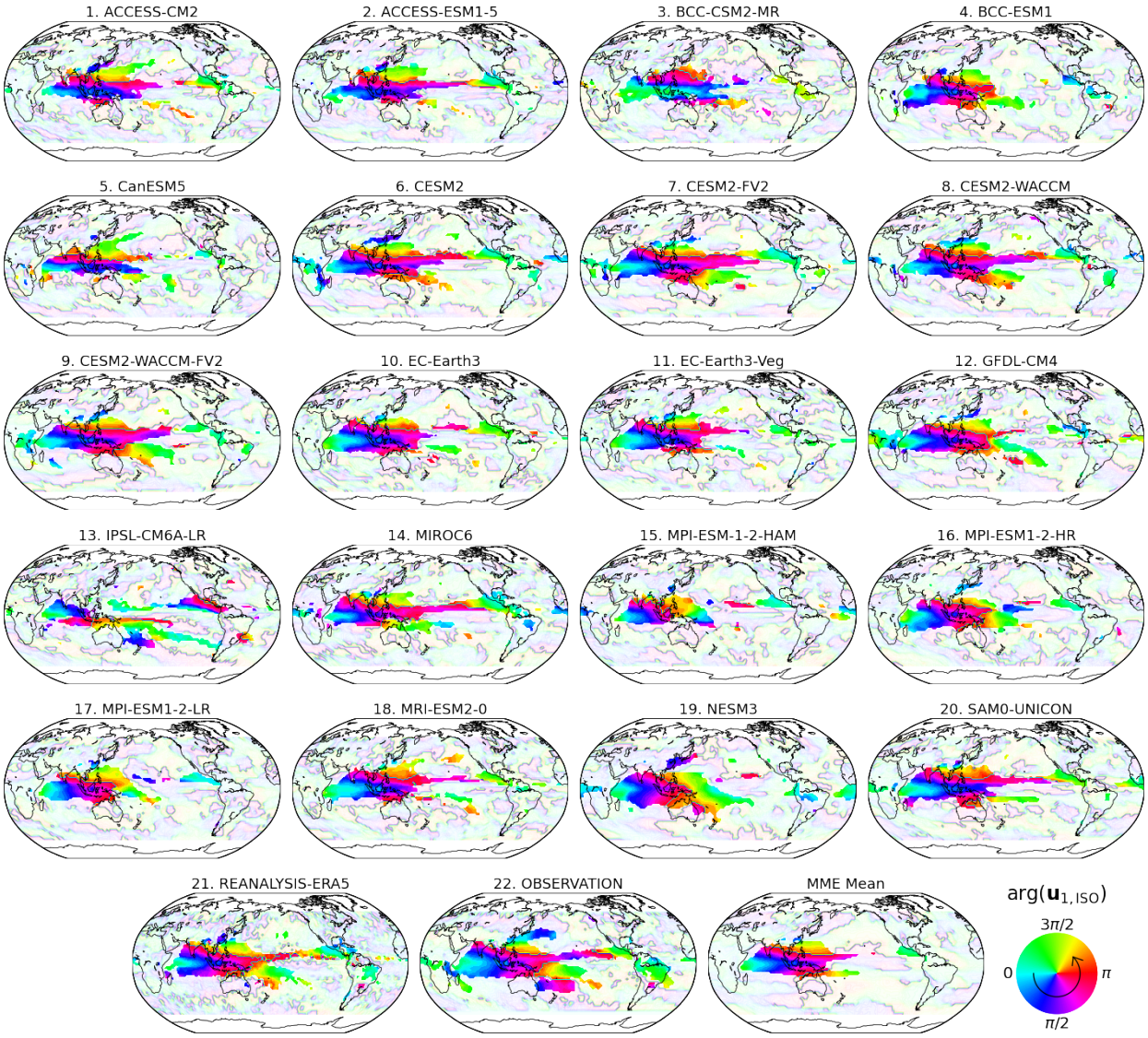

Figure S5. Spatial patterns of the argument (phase) of the MJO band-integrated first complex eigenvector $\boldsymbol{u}_{1,\mathrm{ISO}}$ of PPT, representing MJO propagation, for 20 CMIP6 models, reanalysis, and observations. The MME Mean represents the mean of 20 models. The counter-clockwise, circular arrow in the colorscale indicates the direction of propagation of the extracted waves.

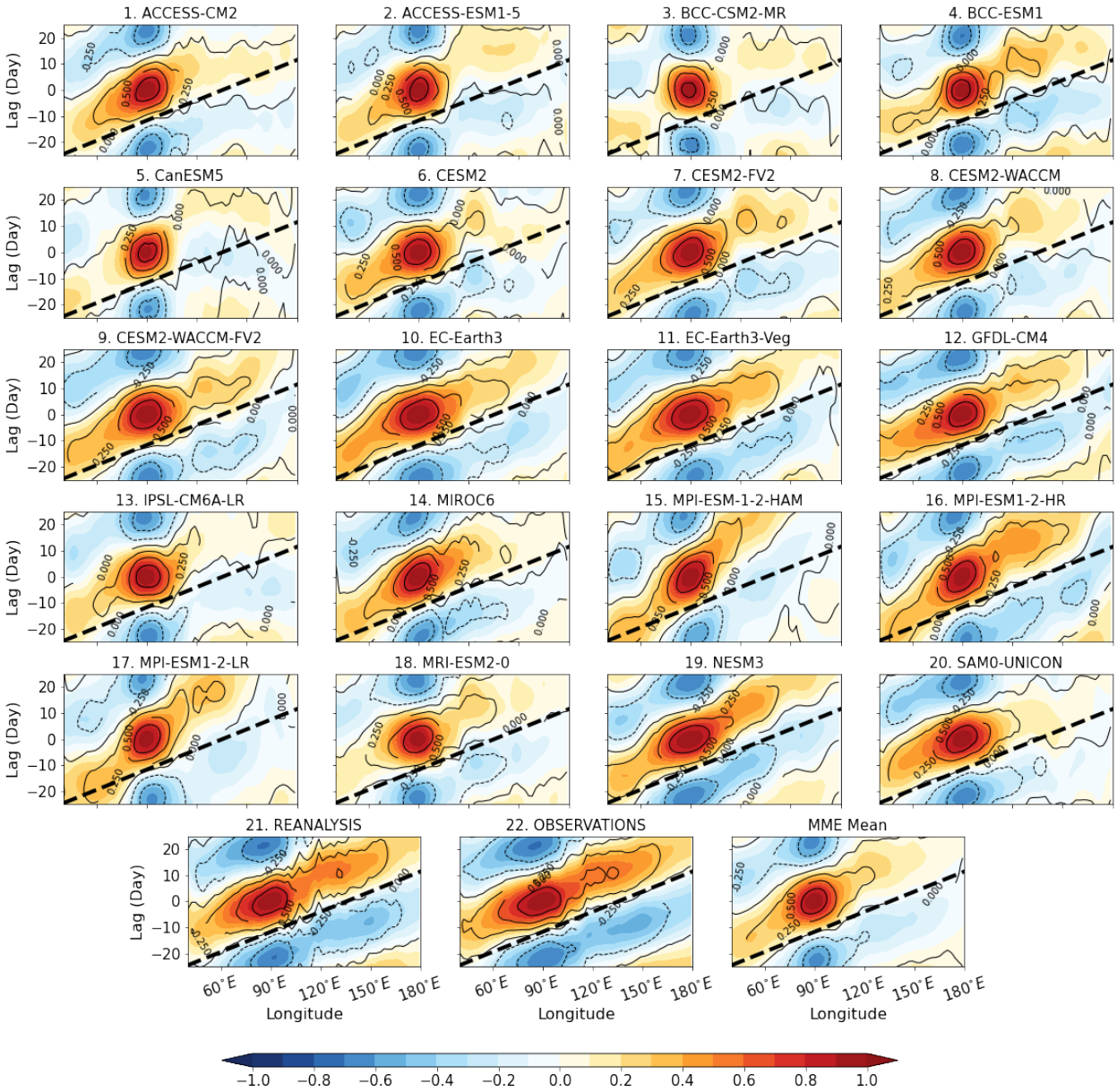

Figure S6. Lag-longitude diagram of 10°S-10°N-averaged OLR anomalies (colors) and PPT anomalies (contours) reconstructed within the ISO frequency band (30-90 days) against the corresponding OLR and PPT anomalies at the Indian Ocean reference region (10°S-10°N, 80°-100°E) from 1983-2014. The reconstruction of OLR and PPT anomalies was performed through inverse wavelet transform of the wPC1 time series $\boldsymbol{\kappa}_{1,f}$ for frequencies f within the ISO frequency band. Black dashed lines indicate an eastward propagation speed of 5 m/s.

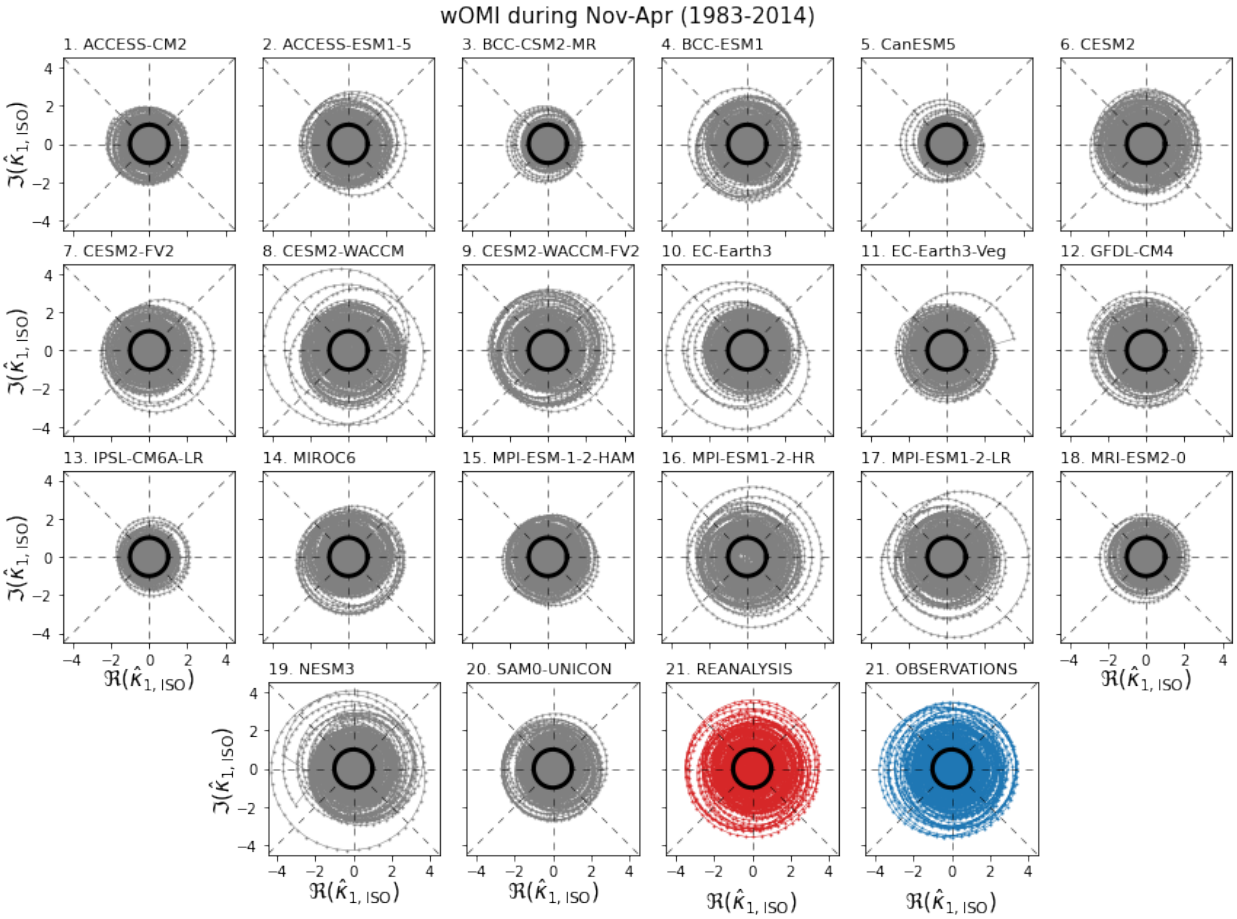

Figure S7. Comparison of wsPCA-based OLR MJO index (wOMI) $\widehat{\boldsymbol{\kappa}}_{1,\mathrm{ISO}}$ reproduced by 20 CMIP6 models, reanalysis products, and observations. The wOMI plots are shown during boreal winter season (Nov-Apr) from 1983-2014. It can be seen that a large number of models underestimate the amplitude of MJO.

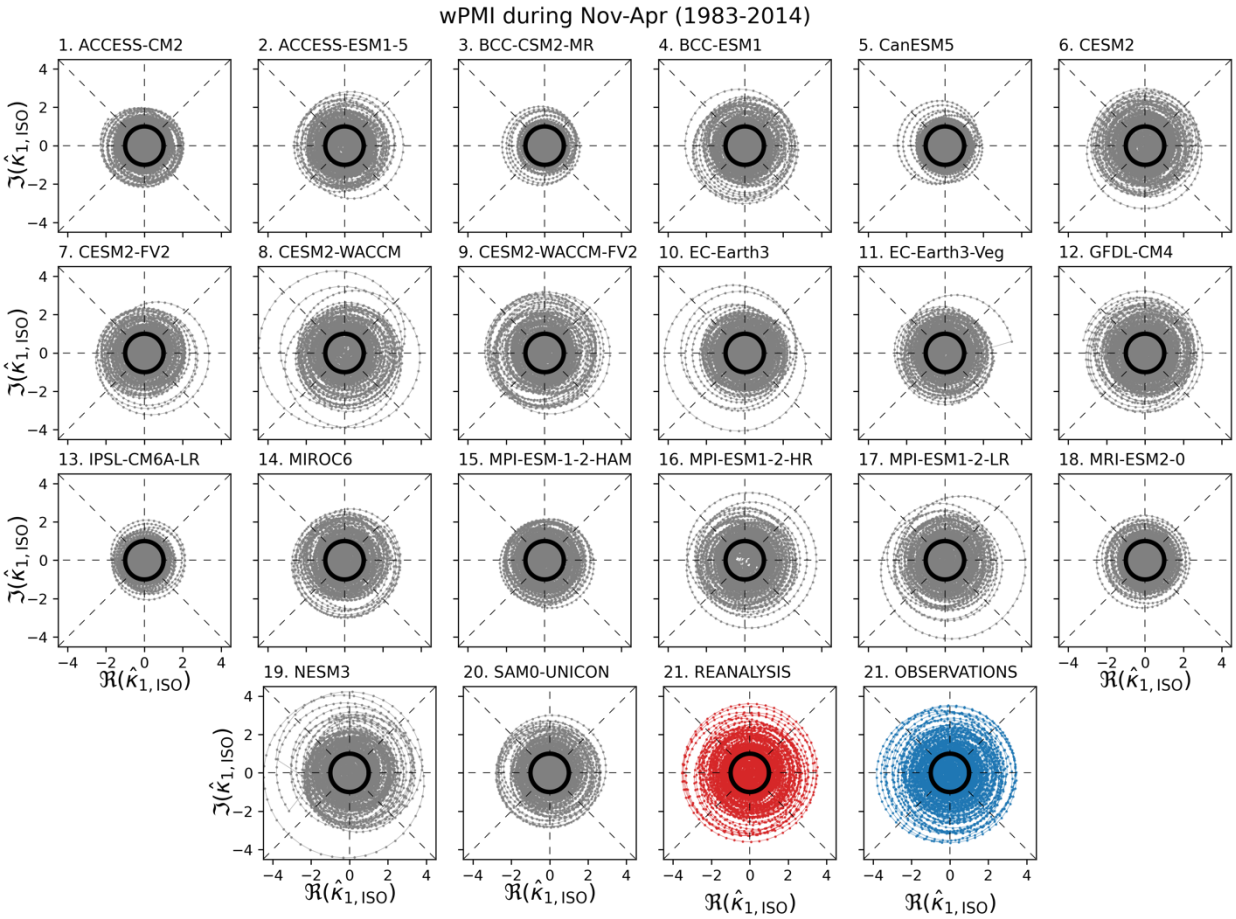

Figure S8. Comparison of wsPCA-based PPT MJO index (wPMI) $\widehat{\boldsymbol{\kappa}}_{1,\mathrm{ISO}}$ reproduced by 20 CMIP6 models, reanalysis products, and observations. The wPMI plots are shown during boreal winter season (Nov-Apr) from 1983-2014. Similar to wOMI, it can be seen that a large number of models underestimate the amplitude of MJO using the wPMI.

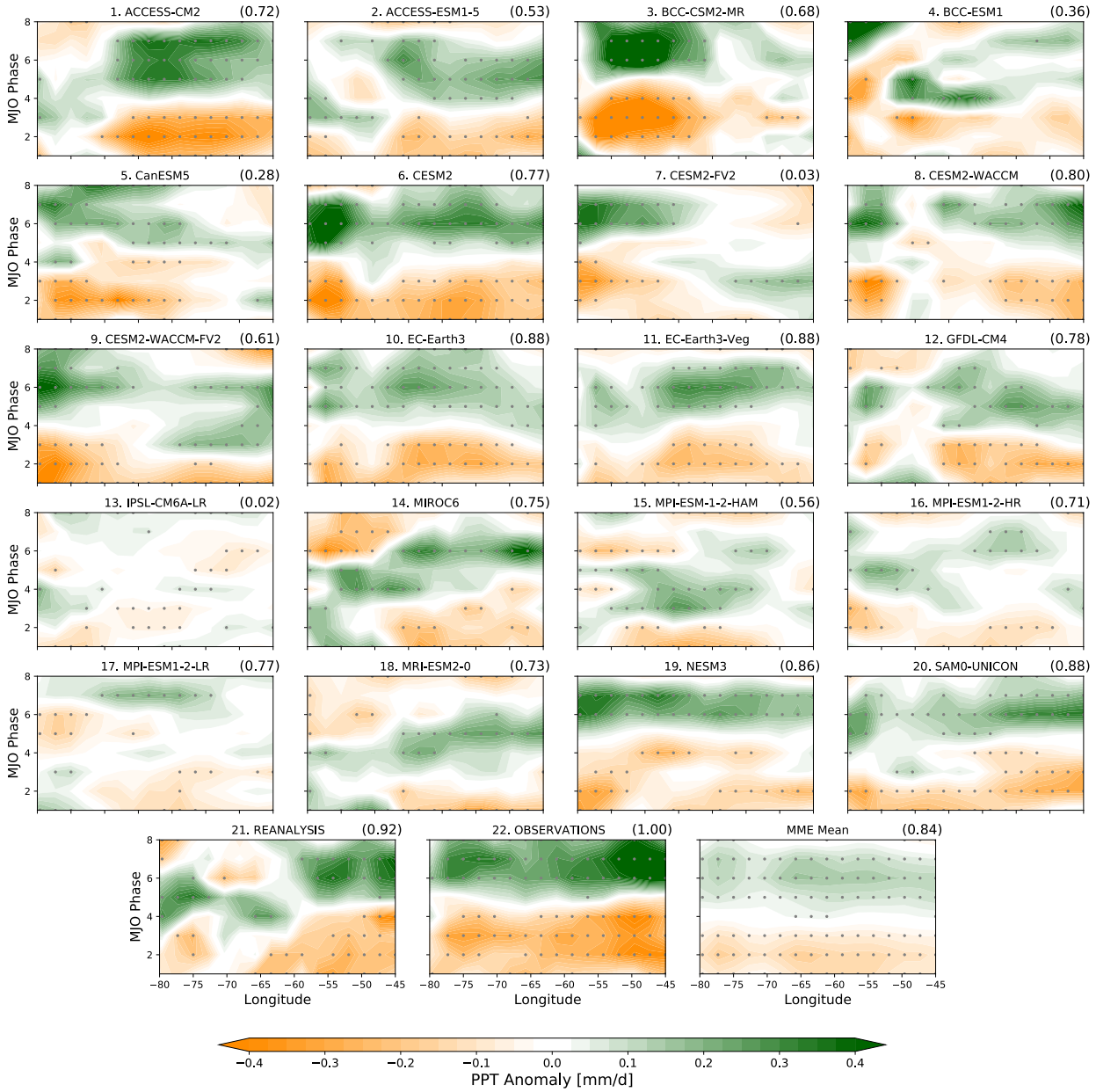

Figure S9. Hovmöller phase-longitude diagrams of PPT anomalies in the Amazonia (10ºN-20ºS, 45ºW-80ºW) for 20 CMIP6 models, reanalysis, and observations. The MME Mean represents the mean of models. The dots indicate statistically significant anomalies ($p<0.05$). Numbers in parentheses represent the correlation coefficients of the phase-longitude patterns with the pattern obtained from the observations.

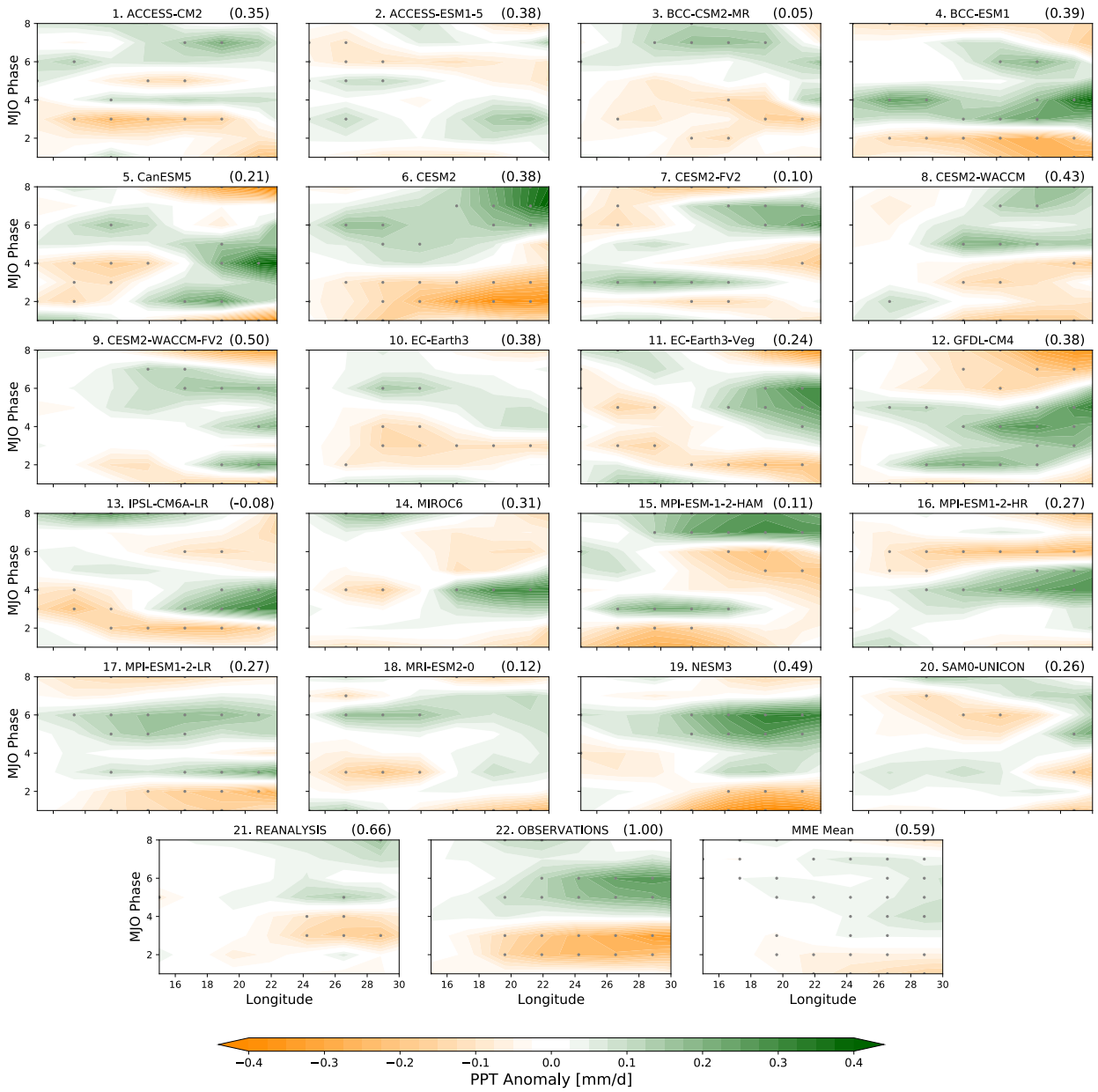

Figure S10. Hovmöller phase-longitude diagram of PPT anomalies in the Southwest Africa (10^{o}S-30^{o}S, 15^{o}E-30^{o}E) for 20 CMIP6 models, reanalysis, and observations. The MME Mean represents the mean of models. The dots indicate statistically significant anomalies ($p<0.05$). Numbers in parentheses represent the correlation coefficients of the phase-longitude patterns with the pattern obtained from the observations.

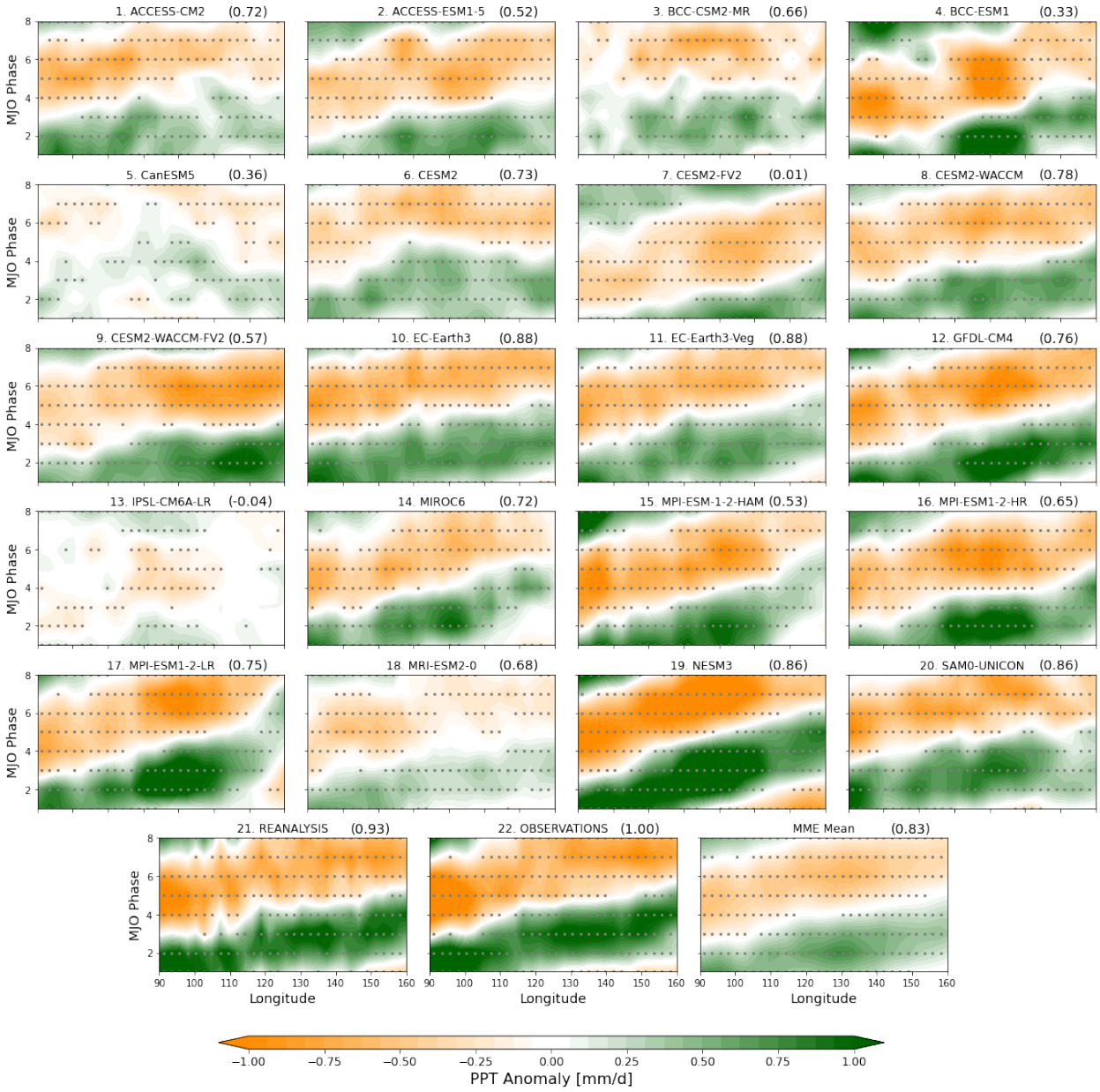

Figure S11. Hovmöller phase-longitude diagram of PPT anomalies in the Maritime Continent (20°S-20°N, 90°E-160°E) for 20 CMIP6 models, reanalysis, and observations. The MME Mean represents the mean of models. The dots indicate statistically significant anomalies ($p<0.05$). Numbers in parentheses represent the correlation coefficients of the phase-longitude patterns with the pattern obtained from the observations.